Ferri-chiral compounds with potentially switchable Dresselhaus spin splitting

Pu Huang [1,*] Zhiguo Xia [2,*,†] Xiaoqing Gao,[1] James M. Rondinelli [3] Xiuwen Zhang [1,‡] Han Zhang,[4] Kenneth R. Poeppelmeier [5,§] and Alex Zunger [6,∥]

[1]*Shenzhen Key Laboratory of Flexible Memory Materials and Devices, College of Physics and Optoelectronic Engineering, Shenzhen University, Shenzhen 518060, China*

[2]*State Key Laboratory of Luminescent Materials and Devices and Institute of Optical Communication Materials, South China University of Technology, Guangzhou 510641, China*

[3]*Department of Materials Science and Engineering, Northwestern University, Evanston, Illinois 60208, USA*

[4]*Collaborative Innovation Center for Optoelectronic Science & Technology, Key Laboratory of Optoelectronic, College of Physics and Optoelectronic Engineering, Shenzhen University, Shenzhen 518060, China*

[5]*Department of Chemistry, Northwestern University, 2145 Sheridan Road, Evanston, Illinois 60208-3113, USA*

[6]*Renewable and Sustainable Energy Institute, University of Colorado, Boulder, Colorado 80309, USA*

Spin splitting of energy bands can be induced by relativistic spin-orbit interactions in materials without inversion symmetry. Whereas polar space-group symmetries permit Rashba (R-1) spin splitting with helical spin textures in momentum space, which could be reversed upon switching a ferroelectric polarization *via* applied electric fields, the ordinary Dresselhaus effect (D-1_A) is active in materials exhibiting nonpolar noncentrosymmetric crystal classes with atoms occupying exclusively nonpolar lattice sites. Consequently, the spin-momentum locking induced by D-1_A is not electric field switchable. Here we find a type of ferri-chiral materials with an alternative type of Dresselhaus symmetry, referred to as D-1_B, exhibiting crystal class constraints similar to D-1_A (all dipoles add up to zero), but unlike D-1_A, at least one polar site is occupied. The spin splitting is associated with the crystalline chirality, which in principle could be reversed upon a change in chirality. Focusing on alkali metal chalcogenides, we identify $NaCu_5S_3$ in the nonenantiomorphic ferri-chiral structure, which exhibits CuS_3 chiral units differing in the magnitude of their Cu displacements. We then synthesize $NaCu_5S_3$ (space group $P6_322$) and confirm its ferri-chiral structure with powder x-ray diffraction. Our electronic structure calculations demonstrate it exhibits D-1_B spin splitting as well as a ferri-chiral phase transition, revealing spin splitting interdependent on chirality. Our electronic structure calculations show that a few percent biaxial tensile strain can reduce (or nearly quench) the switching barrier separating the monodomain ferri-chiral $P6_322$ states. We compute the circular dichroism absorption spectrum of the two ferri-chiral orientations and discuss what type of external stimuli might switch the chirality so as to reverse the (nonhelical) Dresselhaus D-1_B spin texture. Our study suggests the design of ferri-chiral crystals as potential spintronic and optoelectronic materials.

I. INTRODUCTION

Spin splitting in nonmagnetic materials arises fundamentally from a few symmetry rules [1] in the presence of spin-orbit coupling (SOC), combining to produce an internal magnetic field that can split energy bands just as an external magnetic field would do. The various forms of spin splitting in noncentrosymmetric (Non-CS) compounds [1] is generally classified into Rashba [2] (R-1) and Dresselhaus [3] (D-1) effects, whereas hidden spin splitting in centrosymmetric compounds [1] corresponds to R-2 and D-2. The allure of such effects lies in the hope that the relevant spin splitting

can be switched by an external operation, to the benefit of spintronic devices. This generally requires some spatial directionality of the underlying effect—such as vector dipolar polarization—that can be manipulated in a device structure. Such directionality is supplied by the R-1 Rashba effect, but not by the conventional D-1 Dresselhaus effect, since atoms occupy nonpolar sites in D-1 crystals. Indeed, the R-1 effect is enabled in Non-CS compounds that have a polar point group due to a nonzero sum of local dipoles from atoms occupying polar sites. Thus, the R-1 effect is associated with a net directional electric dipolar polarization [1,2,4]; once the ferroelectric polarization is switched, e.g., by an electric field, the Rashba spin splitting can be reversed [5]. On the other hand, the traditional Dresselhaus effect [1,3,4] (hereby denoted D-1_A) is enabled in Non-CS compounds where each occupied Wyckoff orbit has nonpolar site symmetry and dipoles add up to zero, as in tetrahedral GaAs. As this D-1_A effect is created by a nondirectional inversion asymmetry, external electric fields cannot reverse the spin texture.

---

*These authors contributed equally to this work.

†xiazg@ustb.edu.cn

‡xiuwenzhang@szu.edu.cn

§krp@northwestern.edu

∥alex.zunger@colorado.edu

Anti-Chiral CS

FEC-1
polar site
Non-CS

FEC-2
polar site
Non-CS

σ^+ σ^-

D-1$_B$
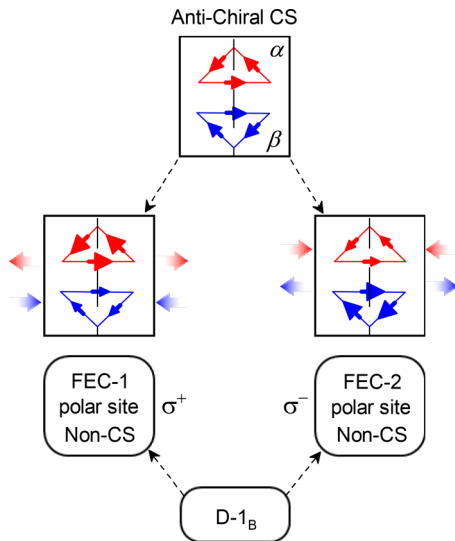
FIG. 1. Schematic depiction of how achiral centrosymmetric (CS) symmetry can decompose into two ferri-chiral (FEC) structures FEC-1 and FEC-2 that are Non-CS. The special case discussed here occurs when the FEC structures exhibit the Dresselhaus effect D-1$_B$, where at least one site has polar symmetry. This behavior is distinct from the standard Dresselhaus effect D-1$_A$ where all sites are nonpolar, as in the zinc-blende structure.

Zhang *et al.* noted [1] that the definition of different bulk spin-splitting functionalities determined by the point-group and space-group symmetries depends on additional aspects of the site symmetries of the individual Wyckoff positions occupied by the atoms in the structure. Although the Dresselhaus effect requires a nonpolar Non-CS crystal class for the space group [6], it can be further differentiated into three subclasses based on the occupied site symmetries in the crystal [1]. In the traditional D-1$_A$ effect each occupied site must be nonpolar, whereas in D-1$_B$ at least one site must be polar, however, the net electric polarization must be zero, i.e., the sum of dipoles arising from local displacements is zero. In contrast, D-1$_C$ polar sites must be occupied, but the sum of dipoles is nonzero. Herein we focus on the D-1$_B$ effect, which although similar to the Rashba effect differs in that there is zero net electric polarization. Chiral crystals with polar individual site symmetries (e.g., LiAlO$_2$) are examples of D-1$_B$ materials which compensate each other even though they are not inversion partners. This special Dresselhaus spin splitting enabled by crystallographic chirality is rarely studied but could also be used to remove the Kramer's degeneracy in crystals with relativistic interactions and access spin-polarized carriers in nonmagnetic compounds.

Here we focus on ferri-chiral materials, where two sets of chiral units differentiated by opposite distortion senses cannot exactly compensate each other (Fig. 1). The direction of these small atomic displacements governs the spin-split electronic band structure, which can be reversed upon changing the orientations of these units. We identify NaCu$_5$S$_3$ as a stable ferri-chiral compound by symmetry screening in the diverse family of alkali metal copper chalcogenides followed by analysis of the spin splitting in the electronic structure with density functional calculations. We then synthesize NaCu$_5$S$_3$ and computationally demonstrate that the Dresselhaus spin

splitting is interlocked with its ferri-chirality. We show that application of modest strain significantly reduces the barrier between the two orientations of ferri-chiral NaCu$_5$S$_3$. We discuss features of various external stimuli that might switch the chirality and reverse the (nonhelical) Dresselhaus D-1$_B$ spin texture, offering an alternative to the traditional reversal of the (helical) Rashba spin texture.

II. THEORETICAL SEARCH FOR FERRI-CHIRAL COMPOUNDS OF TYPE D-1$_B$

We search for compounds that satisfy the basic design principles for ferri-chiral D-1$_B$ Dresselhaus spin splitting. These design constraints include: (i) the material is chiral with nonpolar and noncentrosymmetric space groups; (ii) at least one atomic site in the unit cell of the crystal has polar site symmetry; (iii) the transition barrier between the two chiral phases is sufficiently low (e.g., does not require bond breaking); and (iv) the material is thermodynamically stable (i.e., does not phase separate).

Regarding the last condition, we previously advanced an approach to search for materials that are stable and likely synthesizable by constructing the chemical potential polygon [7–9] in the relevant elemental chemical potential space. This process relies on finding whether there is a region ("green zone") where none of the possible competing phases will render the targeted phase unstable. Details of the density functional theory used are given in Appendix A. Application to the equiatomic ($p = q = r = 1$) ternary $A_pB_qX_r$ 18-electron phases has previously shown numerous [7,10], never before made compounds that were subjected to the search of target functionalities and selective synthesis [Figs. 2(a)–2(c)]. Here we extend the search of stable new phases to general, i.e., nonequiatomic, stoichiometries (p, q, r) of the ternary {A, B, X} family with A^I, B^I, and X^{VI}, filtering compounds that fulfill the conditions for ferri-chiral D-1$_B$ Dresselhaus spin splitting.

To find the lowest energy crystal structure of a missing compound (e.g., NaCuS), we construct a set of candidate crystal structures for its composition from those that are known for existing compounds in ICSD [11], such as AgMgAs-type (F-43m), LiGaGe-type ($P6_3mc$), and ZrBeSi-type ($P6_3/mmc$) structures for 1:1:1 composition, and compute the total energy of each missing material in each structure subject to local relaxations, and then select from this list the lowest energy structure [12]. For the reported compounds, we use the experimentally determined crystal structures. To determine the thermodynamic stability of a target ternary compound $A_lB_mX_n$, we consider all of its possible disproportionation channels to competing phases (elemental phases, binaries and ternaries) with neighboring compositions. This is done by solving a set of inequalities in a three-dimensional space of chemical potentials $\Delta\mu_A$, $\Delta\mu_B$, and $\Delta\mu_X$. For all competing elemental phases, we used inequalities of the form $\Delta\mu_I(I = A, B, X) < 0$. For all competing binary phases A_pB_q, we used the inequalities $p\Delta\mu_A + q\Delta\mu_B < \Delta H_f(A_pB_q)$. For all competing ternary phases $A_pB_qX_r$, we used $p\Delta\mu_A + q\Delta\mu_B + r\Delta\mu_X < \Delta H_f(A_pB_qX_r)$. This three-dimensional space of chemical potentials was reduced to two dimensions by the $l\Delta\mu_A + m\Delta\mu_B + n\Delta\mu_X = \Delta H_f(A_lB_mX_n)$ equation. The values of $\Delta\mu_A$ and $\Delta\mu_B$, where all inequalities
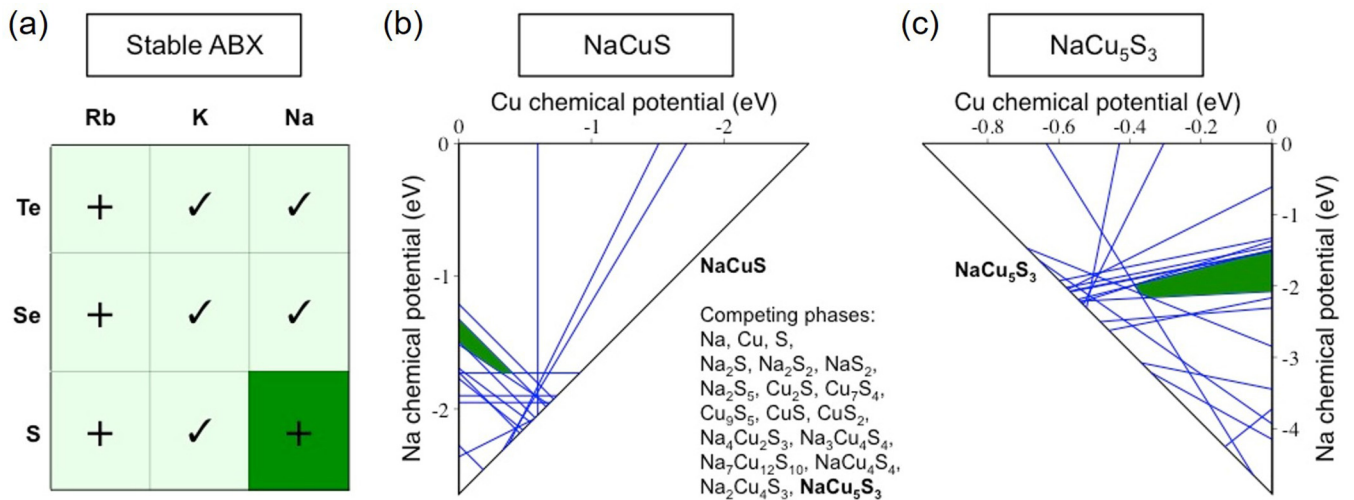
FIG. 2. Stability assessment of alkali metal copper chalcogenides. (a) Predicted (+ signs) and previously reported (check marks) I-I-VI compounds. (b), (c) Stability regions (green zones) of NaCuS and $NaCu_5S_3$ in the space of elemental chemical potentials. Each blue line indicates a binary or ternary competing phase. The areal size of the stability regions (in units of eV^2) for NaCuS and $NaCu_5S_3$ are 0.080 and 0.287, respectively, compared to the other ternary compounds in the Na-Cu-S system: $Na_4Cu_2S_3$ (0.175), $Na_3Cu_4S_4$ (0.083), $Na_7Cu_{12}S_{10}$ (0.052), $NaCu_4S_4$ (0.037), and $Na_2Cu_4S_3$ (0.003).

are satisfied, define the stability area of the $A_lB_mX_n$ compound.

Our analysis of sodium thiocuprates in the Na-Cu-S system shows several previously made I-I-VI compounds indicated by checkmarks in Fig. 2(a), and previously unknown compounds predicted here are stable (denoted by + sign; subsequently realized in experiments [13,14] except NaCuS). Appendix B lists the predicted as well as previously known alkali metal copper chalcogenides. According to structural symmetry analysis, we identify one compound ($NaCu_3Te_2$) with a polar space group permitting R-1 spin splitting, three materials (NaCuS, KCuSe, and KCuTe) with hidden spin

polarization (D-2) effect [1], and 26 compounds (e.g., KCu_3Te_2) with the R-2 and D-2 effects [1]. We identify among alkali metal copper chalcogenides one candidate compound $NaCu_5S_3$ that possesses the structural symmetries required for the D-1$_B$ effect.

We evaluated the thermodynamic stability of the candidate material $NaCu_5S_3$ against disproportionation into its competing phases, as well as those of the other ternaries in the Na-Cu-S system, to examine the synthetic feasibility. Our results show that $NaCu_5S_3$ exhibits the largest stability (green) zone [0.287 eV^2, Fig. 2(c)]; it is a few times larger than those of NaCuS [0.08 eV^2, Fig. 2(b)] and the other ternaries.
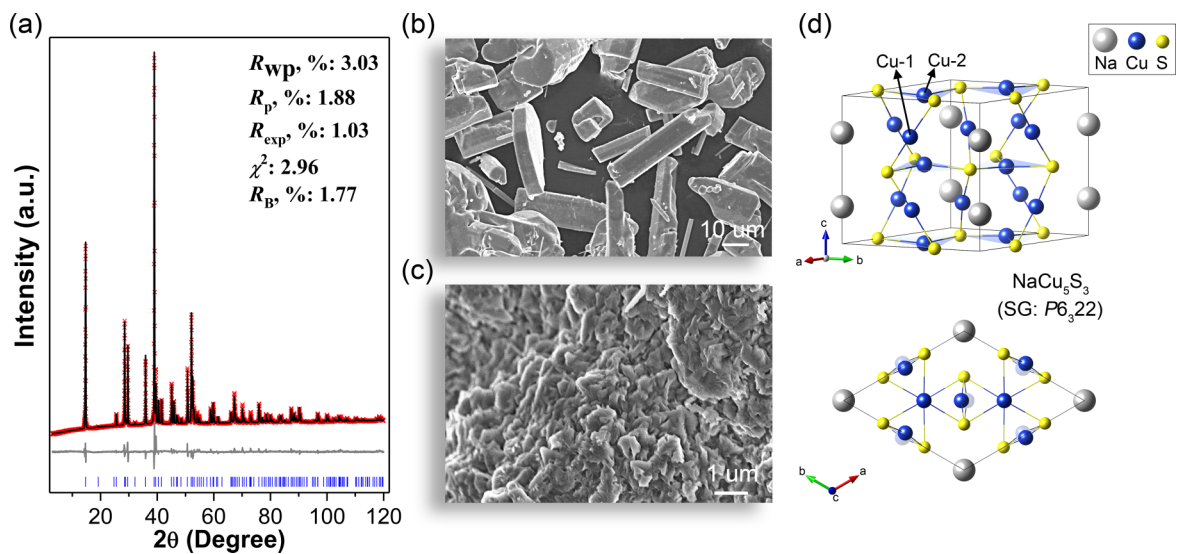
FIG. 3. Experimentally synthesized $NaCu_5S_3$. (a) Rietveld fit to PXRD data. (b) Typical SEM image of as-prepared $NaCu_5S_3$ microcrystals. (c) SEM image of bulk $NaCu_5S_3$ obtained by the SPS sintering at 500 °C with high relative density of 96%. (d) Crystal structure of $NaCu_5S_3$ ($P6_322$) with two unique Cu atoms (Cu-1 and Cu-2). One Cu-1 (Cu-2) atom becomes another under the C_3 (C_2) symmetry operation with the rotation axis coinciding with the Cu-2 (Cu-1) sites.
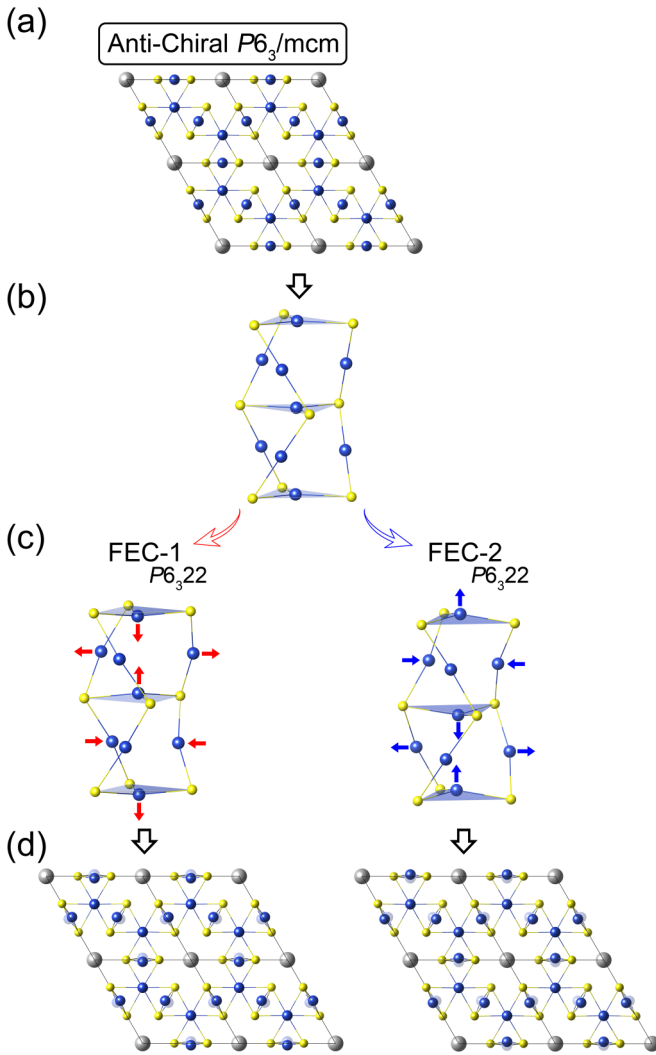
FIG. 4. Schematic representation of the symmetry evolution for $NaCu_5S_3$. (a), (b) Antichiral (AC, fully compensated opposite chiralities). (c), (d) Ferri-chiral (FEC, partially compensated opposite chiralities) orientations 1 and 2. The "twisted triangular prism" consists of two CuS_3 and three CuS_2 motifs constituting the structural chiral unit. FEC-1 is used in DFT struture relaxations, and FEC-2 is deduced from FEC-1 by an inversion transformation.

Our first-principles thermodynamic data agree well with the previous synthesis [15–20] of Na-Cu-S compounds, and the calculated sizes of stability zones suggest that the synthetic feasibility of $NaCu_5S_3$ is the highest among all Na-Cu-S compounds.

III. SYNTHESIS AND CRYSTALLOGRAPHIC ANALYSIS

A. Synthesis

Six sodium thiocuprates in the Na-Cu-S system, including $NaCu_5S_3$, $NaCu_4S_4$, $Na_2Cu_4S_3$, $Na_3Cu_4S_4$, $Na_4Cu_2S_3$, and $Na_7Cu_{12}S_{10}$ [15–20], were generally prepared by melting mixtures of the following three products in different ratios of sodium metal (sodium sulfide, Na_2S), copper (copper sulfide, Cu_2S), and sulfur powder. Reagent chemicals were used as received: NaOH flake (98%, Alfa Aesar), Cu_2S (99.5%, Alfa
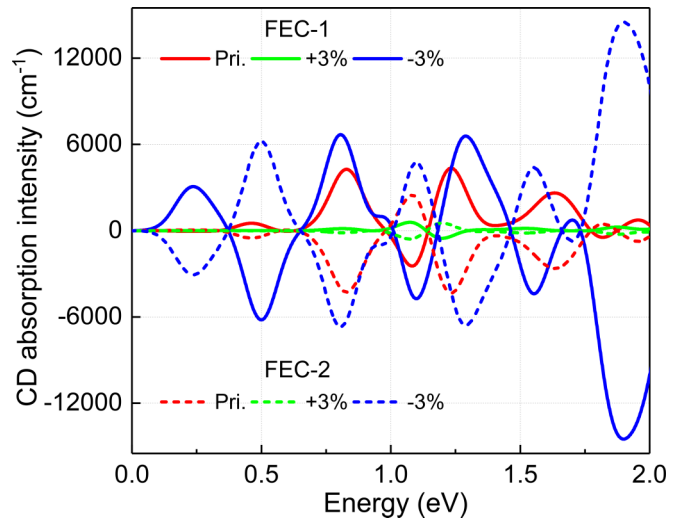
FIG. 5. Simulated circular dichroism absorption spectrum of the pristine and strained FEC-1 and FEC-2 orientations of $NaCu_5S_3$.

Aesar), thiourea (99%+, Sigma-Aldrich), and ethanediamine ($\geqslant$99%, Sigma-Aldrich).

We prepared $NaCu_5S_3$ microcrystals by using the solvothermal method and ethanediamine as the solvent. $NaCu_5S_3$ was first reported by Effenberger and Pertlik [15] in 1985 via the hydrothermal synthesis from the starting materials of Cu powder and Na_2S in H_2O. Here we prepared the $NaCu_5S_3$ microcrystals by a facile solvothermal method. In our typical procedure, 3.125 mmol Cu_2S, 0.625 mmol thiourea, 12.5 mmol NaOH (tenfold excessive stoichiometry), and 6 mL ethanediamine were added in a 3×1.75 in. rectangle Teflon pouch. Then six Teflon pouches were placed in a 100-mL Teflon-lined Parr pressure vessel filled with 50 mL of deionized H_2O as backfill. Pressure vessels were heated to 200 °C for 24 h and cooled to room temperature naturally. Pouches were opened in air, and the microcrystal products were recovered *via* vacuum filtration and the following drying in a vacuum furnace at 60 °C for 12 h.

B. Characterization

The phase purity of the products was assessed by powder XRD (PXRD). The products were finely ground and mounted on a flat-plate sample holder. Diffraction data were collected on a Rigaku MiniFlex 600 diffractometer with the Cu $K\alpha$ source, operating at 40 kV and 15 mA under a continuous scanning method in the 2θ range 5°−120°. PXRD data were analyzed with the Rietveld method using the TOPAS 4.2 program. The morphologies of the typical as-prepared $NaCu_5S_3$ microcrystal product and the cracked section of the $NaCu_5S_3$ pellet were performed with a Hitachi S-4700-II scanning electron microscope.

Electrical conductivity measurements were performed on as-prepared $NaCu_5S_3$, and microcrystal products were first densified by the spark plasma sintering (SPS) method (SPS-211LX, Fuji Electronic Industrial Co., Ltd.), which was treated at 723 K for 5 min in a 12.7-mm-diameter graphite die under an axial compressive stress of 40 MPa in vacuum. Highly dense (>95% of theoretical density) disk-shaped
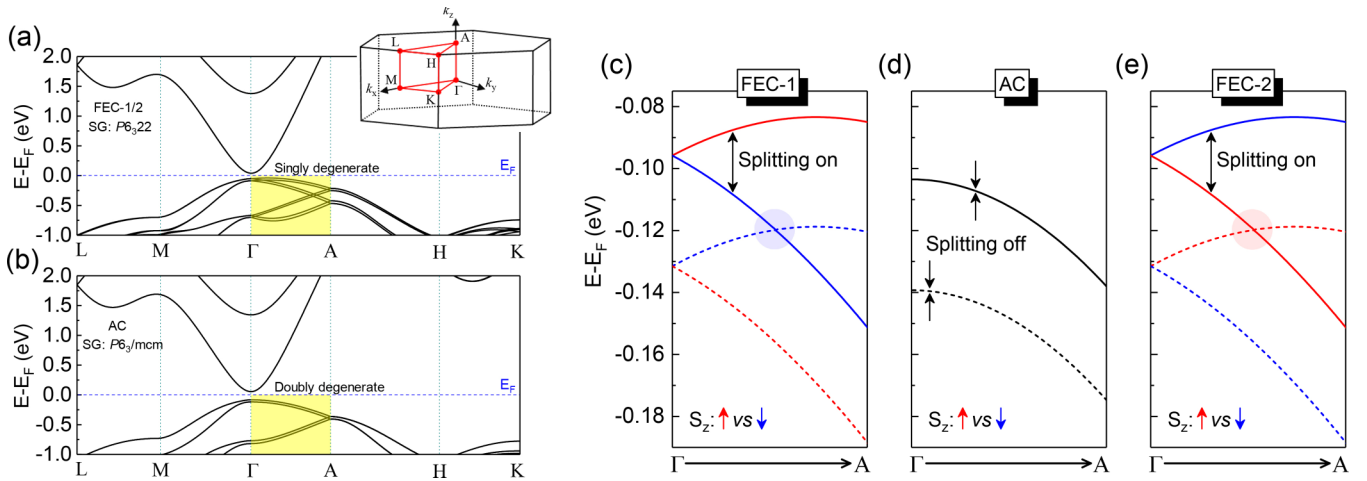
FIG. 6. D-1$_\mathrm{B}$ Dresselhaus spin splitting in NaCu$_5$S$_3$. (a), (b) Band structures for NaCu$_5$S$_3$ with $P6_3 22$ and $P6_3/mcm$ symmetries calculated by DFT + U + SOC. Inset: The Brillouin zone of the hexagonal structures. (c)–(e) Detailed band structure information near the VBM along the $\Gamma - A$ k line for the antichiral (AC) and ferri-chiral (FEC-1 and FEC-2) orientations of NaCu$_5$S$_3$. Red/blue colors in (c) and (e) indicate the spin projection with the spin polarization axis along the z direction.

pellets with dimensions of 12.7-mm diameter and 8-mm thickness were obtained.

C. Crystallographic analyses

Figure 3(a) presents the results of our powder x-ray diffraction measurements. All diffraction peaks were indexed using a hexagonal cell ($P6_3 22$) with parameters close to previously reported NaCu$_5$S$_3$ and the refined lattice constants, $a = 7.0102(1)$ Å, $c = 7.2395(1)$ Å, and volume $V = 308.09(1)$ Å^3. Our Rietveld refinements yielded excellent refinement statistics, $R_{wp} = 3.03\%$, $R_p = 1.88\%$, $R_{\mathrm{exp}} = 1.03\%$, and $\chi^2 = 2.96$, which indicate that the sample was prepared with high phase purity. Well-defined NaCu$_5$S$_3$ crystals varying in size from 30 to 50 μm with rod- and platelike morphologies are observed [see the scanning electron microscopy (SEM) image in Fig. 3(b)], which are consistent with the crystalline habit of the hexagonal crystal system. Exposed to SPS sintering at 500 °C, the NaCu$_5$S$_3$ microcrystals are fractured into smaller uniform ones with 2–3-μm diameters in size [Fig. 3(c)]. We observe compact packing after the SPS process, which supports the high relative density of 96% calculated by volume and weight.

NaCu$_5$S$_3$ belongs to the class of chiral materials with a nonpolar nonenantiomorphic space group ($P6_3 22$, No. 182), meaning that the same space group can permit structures in two equivalent orientations rather than forming enantiomor-

phic pairs (e.g., $P6_1 22$ and $P6_5 22$). The crystal structure for the experimentally synthesized phase is shown in Fig. 3(d), and the occupied Wyckoff sites are presented in Table I, Appendix C. The important feature emphasized herein, following Zhang *et al.* [1], is that the point-group polarities of individual Wyckoff positions matter: the Na sublattice in NaCu$_5$S$_3$ has the Non-CS and nonpolar point group D_3; the two Cu sublattices host C_3 (polar and chiral) and C_2 (polar and chiral) site symmetries, respectively, and the sum of dipoles on the Cu sublattices is zero. Although the Cu sublattices are individually polar, they cannot contribute to a net polarization because the axis of rotation for the site symmetry is orthogonal to the direction of the displacements permitted by the free parameter in the Wyckoff orbits. This is the key local crystallographic feature that enables the D-1$_\mathrm{B}$ Dresselhaus subclass without unlocking a Rashba-like interaction. Finally, the S sublattice has the polar chiral site symmetry C_2, which also prohibits a net dipole.

We next use these refined experimental structures with additional symmetry analysis to further understand the atomistic origin of the chirality in NaCu$_5$S$_3$, which we show is best referred to as a ferri-chiral (FEC) configuration. NaCu$_5$S$_3$ can exist in two forms: the higher-energy symmetric CS achiral $P6_3/mcm$ structure [Figs. 4(a) and 4(b)], which can transform into one of the two lower-energy FEC-1 and FEC-2 orientations of space group $P6_3 22$ [Figs. 4(c) and 4(d)]. The atomistic displacements that enable the ferri-chirality involve
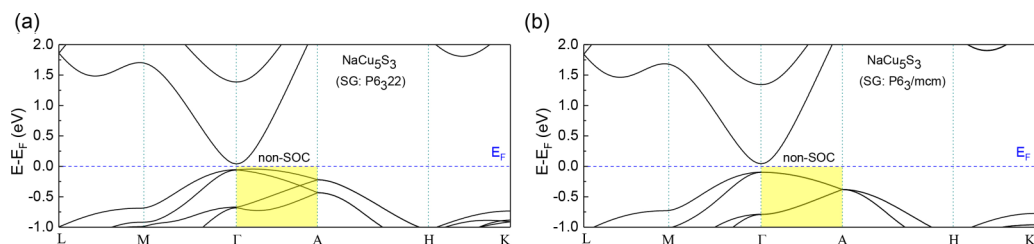
FIG. 7. (a) Band structure of NaCu$_5$S$_3$ with $P6_3 22$ symmetry. (b) Band structure of NaCu$_5$S$_3$ with $P6_3/mcm$ symmetry. Here the band structures were obtained from DFT + U ($U = 6$ eV) without SOC.
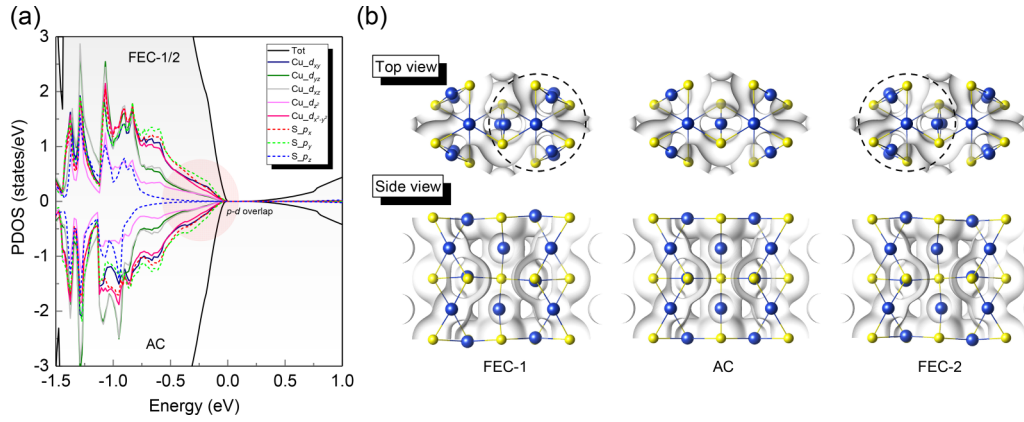
FIG. 8. (a) Partial density of states (PDOS) for $NaCu_5S_3$ with $P6_322$ (FEC-1/2) and $P6_3/mcm$ (AC) symmetries from DFT $+ U$ ($U = 6$ eV) without SOC. (b) Charge densities ($\rho = 0.02\ e\ \text{Å}^{-3}$) of the FEC-1/2 and AC phases.

displacements of Cu-1 in the CuS_2 chain [Fig. 3(d)] and Cu-2 (in the CuS_3 triangle) that transform as the irreducible representation Γ_1^-. Although CuS_2 linear chains have been found in copper chalcogenides [11], CuS_3 planar triangles are an uncommon coordination for copper, which provides a driving force for bond distortion to a nonplanar structure as follows: Cu-1 displaces within the *ab* plane, which removes one mirror plane, whereas Cu-2 displaces along the *c* axis, eliminating the reflection operation perpendicular to the sixfold axis. Chirality arises in this structure because of a perceptual rotation sense due to the antisymmetric displacements on the copper planes, as illustrated for the ferri-chiral phase of $NaCu_5S_3$ with red/blue arrows in Fig. 4(c), which together remove the glide operation. Indeed, these local 3-in-2-out (or 3-out-2-in) displacements exhibit dihedral symmetry; however, their combination results in partial instead of full compensation of the σ^+ and σ^- chiralities to produce the ferri-chiral structures with $P6_322$ symmetry. The chiral motifs and the mechanism of ferri-chirality of $NaCu_5S_3$ are described as follows:

(a) The chiral copper sulfide structural motifs are linearly arranged along the *c* axis in $NaCu_5S_3$ [Fig. 4(b)], with alternating left-handed chirality (σ^+) and right-handed chirality (σ^-). The smallest chiral unit consists of two CuS_3 triangles arranged one above the other with a relative rotation of 60° and the CuS_2 chains connecting their vertices. This chiral unit can be deduced from a triangular prism by a right-handed (left-handed) "twist," hinting at its chirality.
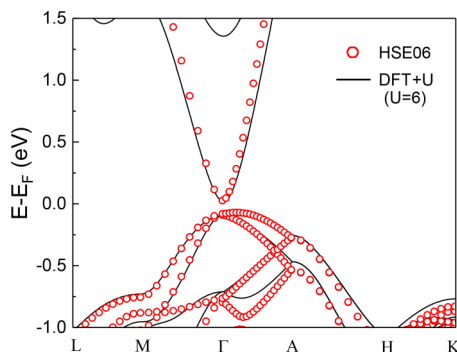
(b) The Non-CS chiral phase of $NaCu_5S_3$ possesses $P6_322$ symmetry and an enantiomorphic point group 622 (D_6). Owing to the sense of the net atomic displacements within the lattice, two chiral configurations (orientations) with $P6_322$ symmetry are possible in the same space group [Fig. 4(c)]: the left (right) structure exhibits the σ^- (σ^+) chiral structural units shrinking and the σ^+ (σ^-) chiral structural units expanding, leading to a net ferri-chirality with partially compensated opposite handedness.

(c) The CS achiral phase of $NaCu_5S_3$ as shown in Fig. 4(a) belongs to the $P6_3/mcm$ space group (see Table I for its Wyckoff positions). Since the CuS_3 triangles in the chiral units become ideally planar and the CuS_2 chains evolve into ideally linear geometries, the σ^+ and σ^- units exactly compensate, leading to an achiral CS phase.

Thus the intensity of the crystalline chirality is determined by the magnitude of the structural unit distortion. This is evidenced by the calculated circular dichroism (CD) absorption spectrum of pristine and strained ($\pm3\%$) $NaCu_5S_3$ in Fig. 5. The FEC-1 and FEC-2 structures exhibit opposite strong CD absorption intensities. As the compressive strain is applied on the structure, the discrepancy between the shrunk and expanded units enlarges with less compensated opposite handedness, leading to the increased net ferri-chirality and enhanced CD intensity. In contrast, the compensation for the σ^+ (σ^-) chiral structural units increases prominently when the tensile strain is induced due to the weakened Cu-S bonding distortion deviated from linearity. The evaluated CD behaviors of the FEC-1/2 structures are consistent with our above analysis for the origin of the chirality in $NaCu_5S_3$ and further demonstrate the correlation between the crystalline chirality and the chiral structural unit distortions.

FIG. 9. Comparison of band structures of $NaCu_5S_3$ with $P6_322$ symmetry from HSE06 and DFT $+ U$ ($U = 6$ eV), without SOC.

IV. BAND DISPERSIONS AND SPIN TEXTURES INCLUDING SOC

We next evaluate the spin splitting and spin texture of the ferri-chiral phases of $NaCu_5S_3$ by density functional theory DFT $+ U$ [21,22] with SOC and $U = 6$ eV. The Non-CS $P6_322$ ferri-chiral phase shows strong spin splitting at the top valence bands along the $\Gamma - A$ direction, in contrast to the CS $P6_3/mcm$ achiral phase with no
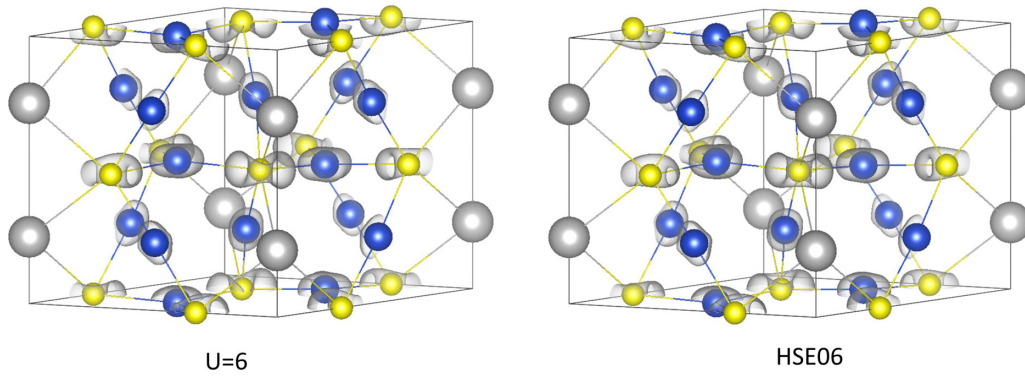
FIG. 10. Comparison for the partial charge densities ($\rho = 0.004\ e\ \text{Å}^{-3}$) at the Γ point of the VBM obtained from DFT $+ U$ ($U = 6$ eV) and HSE06.

spin splitting (Fig. 6). Band structures and electronic densities of states (along with charge densities) obtained without SOC are shown in Figs. 7 and 8, respectively, of Appendix C. Figure 9 compares the band dispersions without SOC obtained using a screened hybrid functional (HSE06 [23,24]) against our DFT $+ U$ results, showing good agreement between the two levels of theory. Figure 10 shows that the partial charge densities at the Γ point of the valence-band maximum (VBM) evaluated with DFT $+ U$ and HSE06 approaches are also in good agreement. Figure 11 shows the effect of different choices of U on the band structure without SOC. Both the spin-splitting magnitude and the linear spin-splitting coefficient are weakly dependent on the Hubbard U used for Cu. The valence-band spin-splitting energy and spin-splitting coefficient are 194/208 meV and 261/275 meV Å for pristine NaCu$_5$S$_3$ with $U = 0/6$ eV, respectively.

Detailed band structures near the VBM in Figs. 6(c)–6(e) show the lifting of the Kramer's degeneracy and the appearance of spin splitting in the ferri-chiral phases, as compared to the CS achiral phase. The overall dependencies of the orbital energy levels in Fig. 6(a) are similar to the electronic structure without SOC (Fig. 7) because of the broken inversion; however, the Kramer's degeneracies are only fully removed in the former case with SOC, which results in spin splitting that is clearly discernable at the VBM along the $\Gamma - A$ direction in Fig. 6(a) [see Fig. 6(c) for the spin notation]. Figure 12 and Appendix C, Fig. 8 show that the following atomic orbitals are

hybridized and mainly contribute to the valence bands along the $\Gamma - A$ direction: S p_x, p_y, Cu-2 $d_{x^2-y^2}$, d_{xy}, Cu-1 d_{yz}, d_{xz}, and d_{z^2}. The contribution of these orbitals in the spin splitting leads to a rather complicated spin texture for the valence band around the Γ point, as shown in Fig. 13.

Although the two ferri-chiral structures possess the same crystalline symmetry, the spin splitting and spin textures are distinct. For the FEC-1 orientation of NaCu$_5$S$_3$, the top two valence bands along the $\Gamma - A$ k path split into four singly degenerate bands with spin polarization along the z direction and individual spin components, showing large linear Dresselhaus spin splitting [Fig. 6(c)] with linear spin-splitting coefficients of ($\frac{1}{2}\frac{dE}{dk} \cong 275$ meV Å). The derived spin-splitting energy for the top valence bands near the A point is $\sim$208 meV, which is remarkably large for the low-atomic-mass elements in NaCu$_5$S$_3$. The large spin splitting of the valence band in NaCu$_5$S$_3$ originates from the distorted Cu-S unit, which eliminates the inversion center of the undistorted antichiral phase ($P6_3/mcm$) and enhances the spin splitting beyond that expected from atomic interactions alone. As a comparison, zinc-blende CuF exhibits modest spin splitting (Fig. 14). Whereas in the FEC-2 phase orientation, the spin splitting is reversed compared to FEC-1, producing completely opposite spin components [Fig. 6(e)]. In other words, the spin splitting switches between the two ferri-chiral phases of NaCu$_5$S$_3$, suggesting that the ferri-chirality is associated with the Dresselhaus spin splitting (D-1$_B$ type), analogous
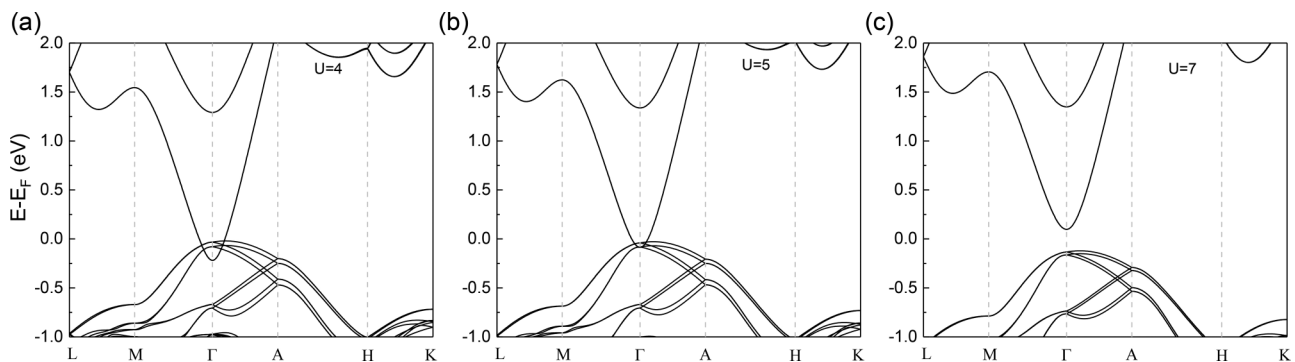
FIG. 11. Band structures of NaCu$_5$S$_3$ with $P6_3 22$ symmetry from DFT $+ U$ without SOC with different U values: (a) $U = 4$ eV, (b) $U = 5$ eV, and (c) $U = 7$ eV.
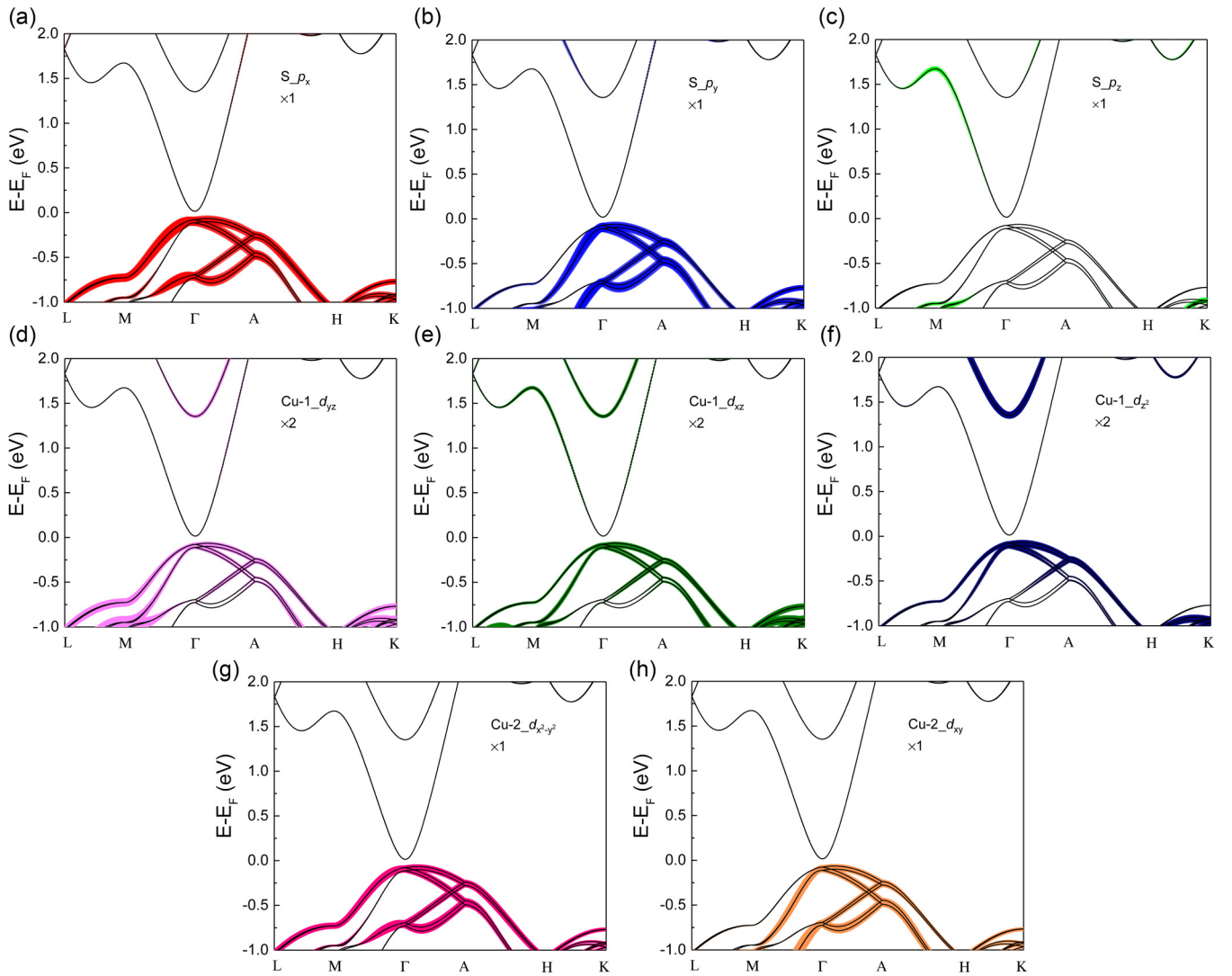
FIG. 12. Atomic and orbital projected band structures (a)–(h) of $NaCu_5S_3$ with $P6_322$ symmetry calculated at the DFT $+ U +$ SOC level.

to the association between dipolar polarization and R-1 spin splitting. Similarly, Fig. 15 shows the spin-split bands in the k_y-k_z plane ($k_x = 0$) with annotated spin polarization directions for the FEC-1 phase, demonstrating the Dresselhaus-like nonhelical spin textures. The spin textures of the top valence bands around the Γ point for a wide k range is shown in

Fig.13, which further demonstrate the Dresselhaus effect and reveal a nearly unidirectional spin texture along k_y for small k. (The corresponding spin texture of FEC-2 phase is opposite to that of FEC-1). Figure 16 shows the spin components of the spin-split bands in the full k range along a k path for FEC-1.
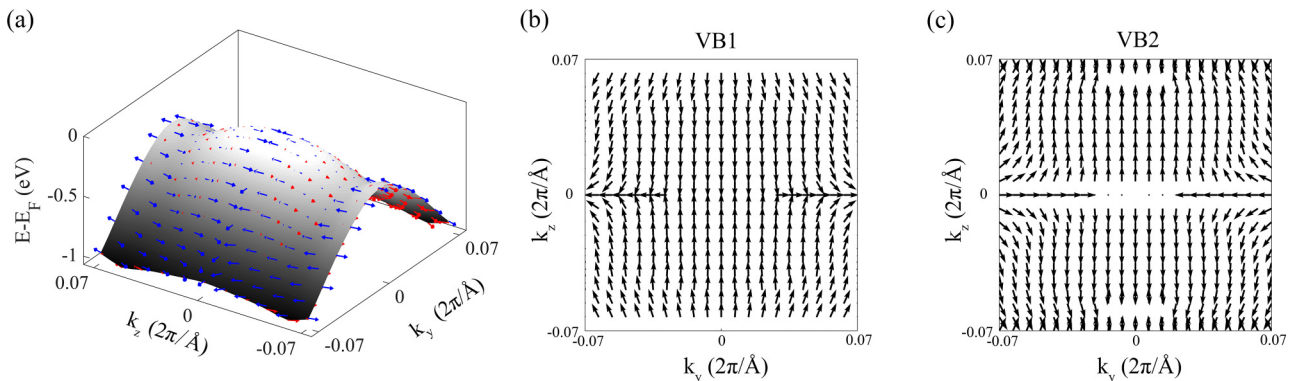
FIG. 13. Spin texture of the FEC-1 structure of $NaCu_5S_3$ in a wide k range around the Γ point for VB1 and VB2 (in comparison to Fig. 15(a) in a narrow k range).
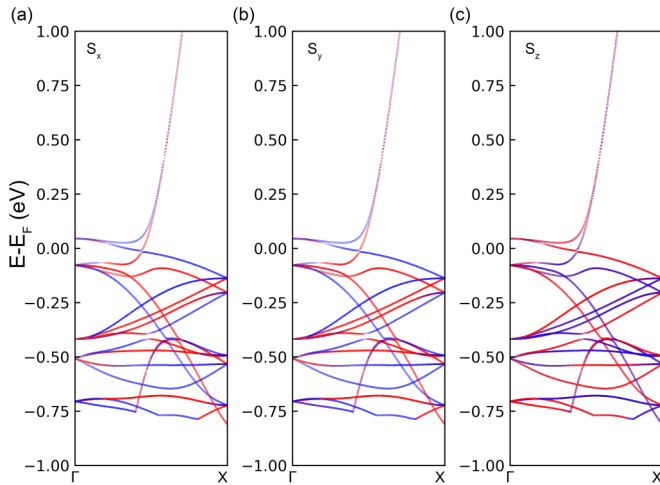
FIG. 14. Band structure of zinc-blende CuF with spin projections.

V. PROSPECTS FOR SWITCHABILITY OF FERRI-CHIRAL SPIN TEXTURE

The ferri-chiral phases in $NaCu_5S_3$ differ only by the chiral unit contracting or expanding without breaking bonds [Figs. 4(c) and 4(d)]. The conversion between the two ferri-chiral phases [indicated by the red/blue arrows in Fig. 4(c)] involves only small atomic displacements but not breaking of chemical bonds, as in a reconstructive transformation. Thus the transition barrier between the two orientations could be rather low for the monodomain state transformation. We assess computationally the transition barrier from FEC-1 to FEC-2. The calculated transition barrier between FEC-1 and FEC-2 is as low as ∼12 meV/f.u., as indicated by the black dashed curve (unstrained case) in Fig. 17(a).

Yet, unlike the case in R-1 compounds, here a static and conventional electric field alone cannot switch the polarization. Another switching agent needs to be identified. At this time we note that switching of chirality in molecular materials has been realized in experiments using external stimuli such as photoexcitation [25–27], electron tunneling [28], and electric fields [29]. On the other hand, chirality-selective synthesis, i.e., chiral induction, was applied to both molecular materials [30–32] and inorganic crystals [33] by using circular polarized light. Furthermore, circularly polarized x-rays [34] and light [35–37], as well as an optical vortex [38], were widely used to probe/manipulate material chirality. Recently, circularly polarized light-induced chirality switching has been realized in metal-inorganic plasmonic nanostructures [39]. Whether these approaches can be used or new avenues advanced for switching $NaCu_5S_3$ is a challenge area for future research.

The ferri-chiral transition barrier can be tuned to zero by a few percent biaxial tensile strain [Fig. 17(a)], indicating thin-film, device-relevant geometries of $NaCu_5S_3$, probed with electrical measurements or optical spectroscopies are a promising strategy to demonstrate the ferri-chiral dependent spin splitting but not necessarily switch it. Table II in Appendix C lists a potential substrate material for imposing tensile strain on $NaCu_5S_3$, which may be grown using pulse-laser deposition from ceramic targets produced using our synthesis strategy. For large enough biaxial tensile strain (∼3%), the atomic
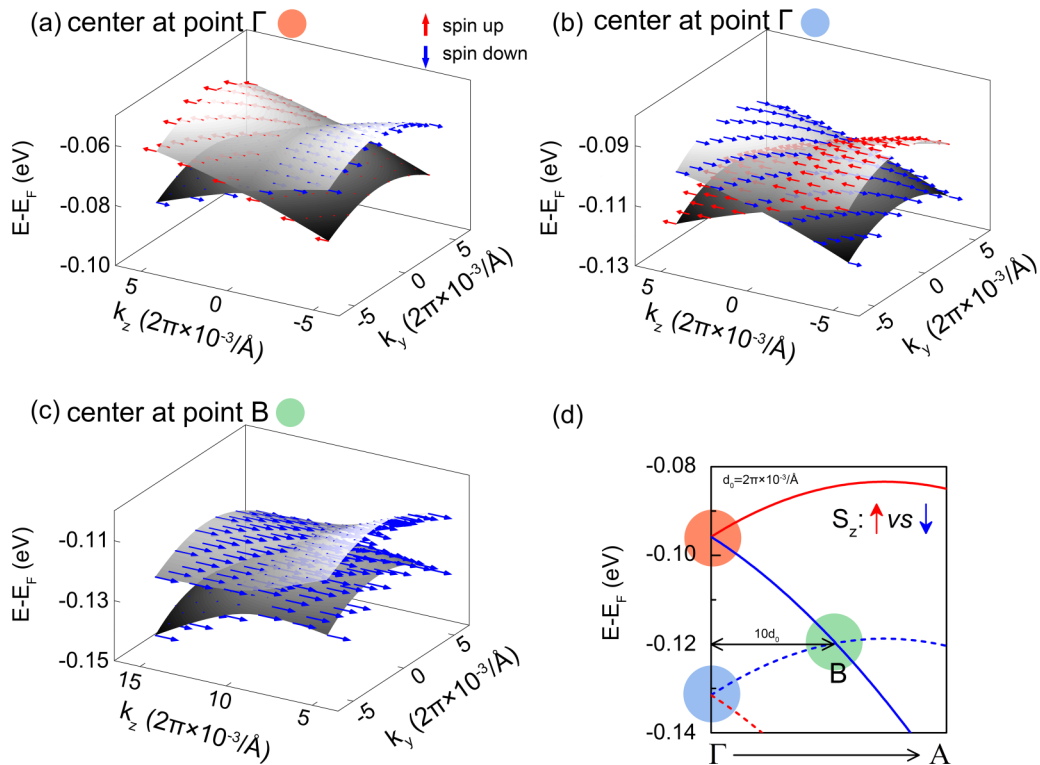
FIG. 15. Spin textures on the (k_y, k_z) plane ($k_x = 0$) for the top valence bands of $NaCu_5S_3$ ($P6_322$) at the DFT + U + SOC level. (a)–(c) Spin textures for different ranges of valence bands. (d) Zoom-in band structure showing the three chosen ranges of valence bands to illustrate the spin texture.
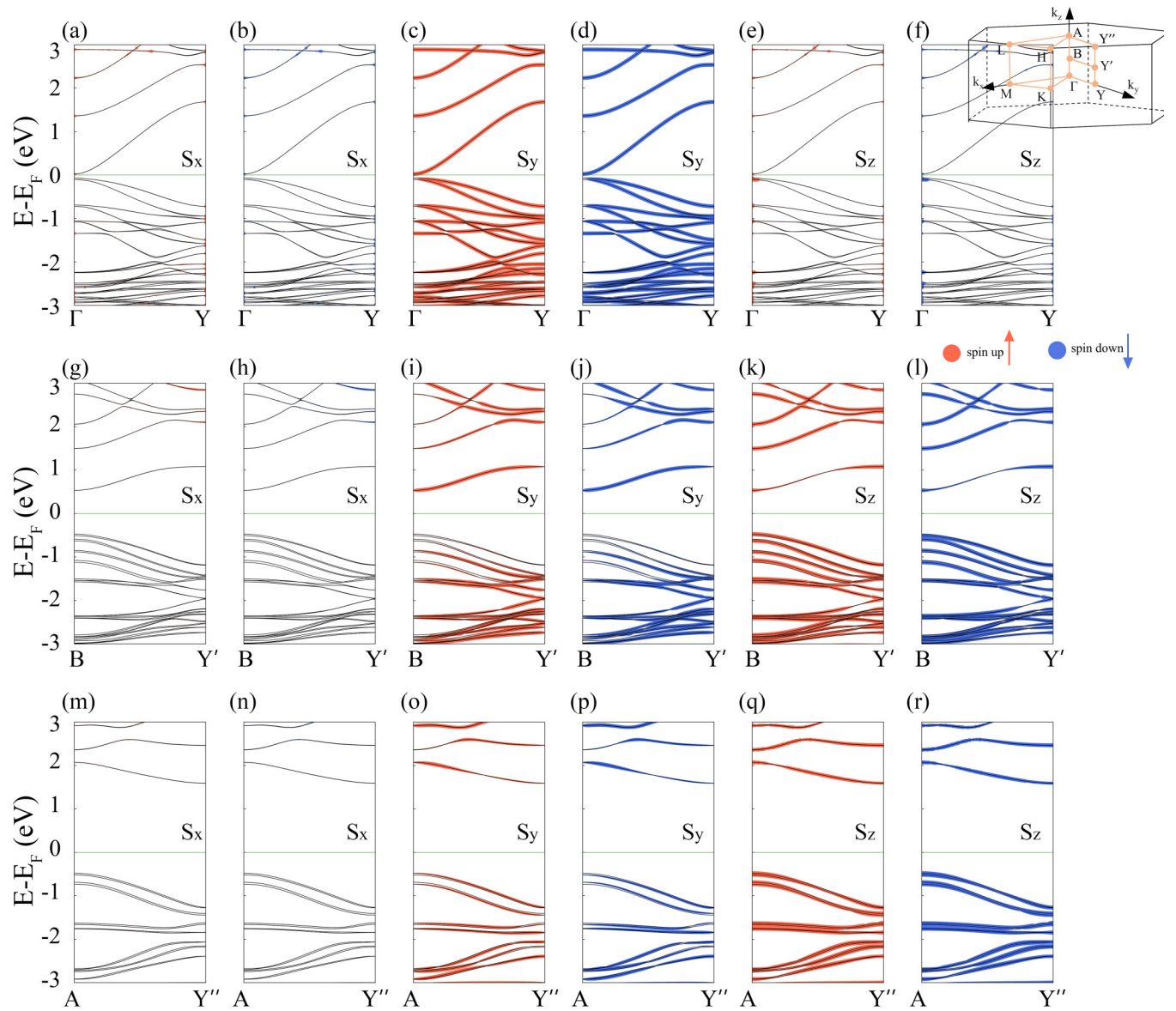
FIG. 16. Spin components of the energy bands in the FEC-1 structure of $NaCu_5S_3$ along $\Gamma - Y$, $B - Y'$, and $A - Y''$ k paths. Inset: Brillouin zone of $NaCu_5S_3$ illustrating the $\Gamma - Y$, $B - Y'$, and $A - Y''$ k paths.

displacements that break the full compensation of σ^+ and σ^- chiralities can be restored [see the variation of the crystallographic parameters in Fig. 17(b)] and the CS antichiral phase ($P6_3/mcm$) is stabilized as the ferri-chiral transition barrier is quenched. Figure 5 also shows that the CD absorption intensity can be significantly decreased (increased) by applying biaxial tensile (compressive) strain.

The ferri-chirality and D-1_B Dresselhaus spin splitting in $NaCu_5S_3$ are inherently interlocked. Figures 6(c) and 6(e) demonstrate the switch of the spin splitting once the chirality is reversed. Furthermore, the D-1_B effect is due to a convergent effect of the atomic-site dipolar polarizations (that sum to zero in the ferri-chiral structure) and thus depends on their relative positions and magnitudes. For that reason, the D-1_B spin splitting could be much more sensitive to crystallographic parameters than the D-1_A effect—this sensitivity could offer

new knobs to manipulate the electron's spin. Figures 17(c) and 17(d) show that the spin-splitting energy near the A point of $NaCu_5S_3$ can be tuned from 16 meV under 3% tensile strain along the c lattice direction to 435 meV under 3% compressive strain. As to the biaxial strain in the ab plane, along with the significant modulation of the chirality-enabling atomic displacements [Fig. 17(b)], a range of spin-splitting energies from zero spin splitting to ∼200% relative to the unstrained case near the A point can be obtained. Figure 18 shows the variation in the electronic structures of $NaCu_5S_3$ under biaxial/uniaxial strains along a/b lattice directions. The calculated strong strain modulation effect of D-1_B spin splitting further demonstrates the interlocking of ferri-chirality and the Dresselhaus effect in ferri-chiral materials, which could offer chirality-related modalities to manipulate/detect spin splitting or vice versa.
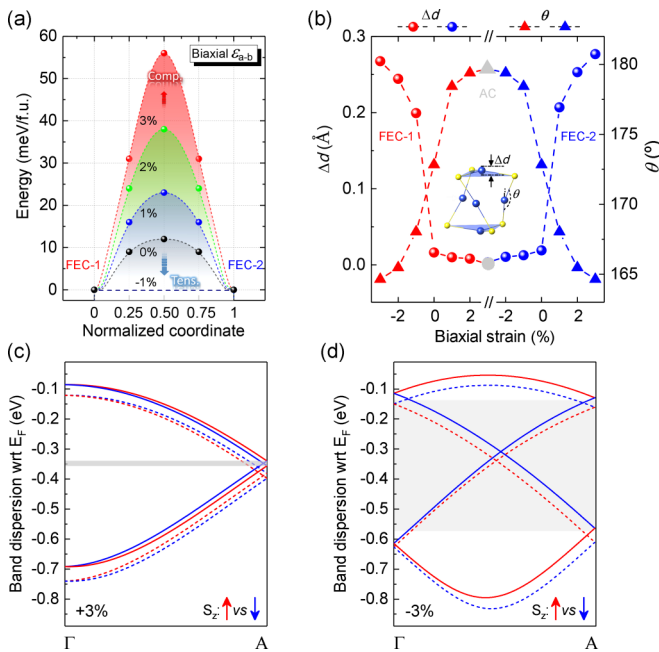
FIG. 17. Tunable ferri-chiral phase transition and spin splitting in $NaCu_5S_3$. (a) Transition barrier between the two ferri-chiral phases of $NaCu_5S_3$. The black dashed curve corresponds to the unstrained case, and other curves correspond to different strain values. (b) Detailed crystallographic information including the movement of Cu-2 away from the center of the CuS_3 planar triangle along [001] lattice direction (Δd), the movement of Cu-1 away from the center of the CuS_2 linear chain as represented by the S-Cu-S angle (θ), and along the transition between FEC-1/2 and AC states under external biaxial strain in the ab plane. The +/- signs represent tensile and compressive strain. (c), (d) Low-energy valence bands in the $\Gamma-A$ direction for the FEC-1 ferri-chiral phase of $NaCu_5S_3$ under uniaxial strain along the c lattice direction. Red/blue colors indicate the spin projection, with the spin polarization axis along the z direction. The gray background indicates the magnitude of the spin-splitting energy. Similar tunability of spin-splitting energy under $a/b/c$ uniaxial/biaxial strains is demonstrated in Fig. 18, in the Appendixes.

FIG. 18. Band structure evolution of $NaCu_5S_3$ (FEC-1) with uniaxial/biaxial strain along $a/b/c$ lattice directions from DFT $+ U$ ($U = 6$ eV) with SOC. The applied strain from left to right is -3%, -1%, 1%, and 3%, respectively, where positive and negative values indicate tensile and compressive strain.

with spin splitting, offering a natural platform to combine mechanical, optical, and spintronic effects.

VI. CONCLUSION

In summary, we designed a type of ferri-chiral material with potentially switchable Dresselhaus spin splitting via a combined theoretical and experimental study. The nonconventional Dresselhaus effect D-1$_B$ found in the experimentally synthesized candidate $NaCu_5S_3$ is interlocked with its ferrichirality, analogous to the association of the Rashba effect with dipolar polarization. The ferri-chiral transition barrier can be significantly lowered or quenched by external strain, facilitating the potential transition between monodomain ferri-chiral states as well as their associated spin splitting by external stimuli, analogous to the chirality switching of metalinorganic nanostructures by circular polarized light [39]. This study initiates the design of novel ferri-chiral materials with potential applications in spintronics and optoelectronics: the Non-CS ferri-chiral phases are active for piezoelectric, nonlinear optics, as well as circularly polarized light that interacts

APPENDIX A: DETAILS OF DENSITY FUNCTIONAL CALCULATIONS

The electronic structure of $NaCu_5S_3$ is evaluated by density functional theory (DFT) [40] using the projector-augmented wave (PAW) pseudopotentials [41] with the exchange cor-relation of Perdew-Burke-Ernzerhof (PBE) form [42] as implemented in the Vienna *Ab-initio* Simulation Package (VASP [41,43]). The electronic wave functions were expanded using a plane-wave basis set with an energy cutoff of 520 eV. The Brillouin zone was sampled on $8 \times 8 \times 8$ Monkhorst-Pack [44] k-point meshes. For the Cu element, we introduced the on-site Coulomb interactions in the localized d orbitals by using the DFT/GGA+U method [21]. The initial crystal structure is taken from experiment, and the lattice constants and atomic positions are fully relaxed under the energy and force tolerance of 10^{-6} eV and 5×10^{-3} eV Å^{-1} per unit cell using a conjugate-gradient (CG) algorithm. Spin-orbit coupling (SOC) effects are taken into account by a per-turbation $\sum_{i,l,m} V_l^{SO} \boldsymbol{L} \cdot \boldsymbol{S} |l, m\rangle_{ii}\langle l, m|$ to the pseudopotential, where $|l, m\rangle_i$ is the angular momentum eigenstate of the ith atomic site [22]. The Wigner-Seitz radii for constructing $|l, m\rangle_i$ used in this study are listed in the pseudopotentials of the VASP simulation package [43]. The spin state of the electron's wave function is evaluated by projecting the calculated wave function $|\phi\rangle$ on the spin and orbital basis of each atomic site $C_{i,l,m,\eta} = \langle\phi|(s_\eta \otimes |l, m\rangle_{ii}\langle l, m|)|\phi\rangle$. The ferri-chiral transformation barriers are evaluated by using the nudged elastic band (NEB) method [45], during which the crystal symmetry and band structure evolution of every image were carefully depicted. We are aware of the DFT band-gap error and compare the band gap obtained from the hybrid functional (HSE06 [23,24]) method with that from DFT + U, and found that DFT + U with $U = 6$ eV on Cu predicts almost the same band-gap value as HSE06. Crystal structures and charge densities were drawn using the VESTA software [46]. The circularly polarized optical absorption was performed with the random phase approximation (RPA) method by decomposing the circularly polarized part $1/\sqrt{2}|\langle\psi_i|\nabla_x \pm i\nabla_y||\psi_j\rangle|^2$ from the total absorption spectrum, as conducted by using the PWMAT code [47,48]. A plane-wave basis set is employed at a cutoff energy of 80 Ry, and a dense k-point mesh of $16 \times 16 \times 14$ over the hexagonal Brillouin zone is sampled during the calculations.

APPENDIX B: PREDICTED AND PREVIOUSLY KNOWN ACHIRAL ALKALI METAL COPPER CHALCOGENIDES

The experimentally reported [11,15] achiral alkali metal copper chalcogenide compounds in the A-B-X systems (A = Na, K, Rb, B = Cu, X = S, Se, Te) are as follows: $Na_4Cu_2S_3$ ($I4_1/a$), $Na_3Cu_4S_4$ ($Pbam$), $Na_7Cu_{12}S_{10}$ ($P2/m$), $NaCu_4S_4$ ($P\bar{3}m1$), $Na_2Cu_4S_3$ ($C2/m$), $NaCu_4Se_4$ ($P6_3/mmc$), $NaCuSe$ ($P4/nmm$), $NaCuTe$ ($P4/nmm$), $NaCu_3Te_2$ ($R3m$), $K_3Cu_8S_6$ ($C2/m$), KCu_4S_3 ($P4/mmm$), $KCuS$ ($Pnma$), KCu_3S_2 ($C2/m$), KCu_2Se_2 ($I4/mmm$), $KCuSe$ ($P6_3/mmc$), $K_3Cu_8Se_6$ ($C2/m$), KCu_4Se_3 ($P4/mmm$), $K_2Cu_5Te_5$ ($Cmcm$), $KCuTe$ ($P6_3/mmc$), $K_4Cu_8Te_{11}$ ($C2/m$), $K_3Cu_{11}Te_{16}$ ($Imma$), KCu_3Te_2 ($C2/m$), $K_2Cu_2Te_5$ ($Cmcm$), $RbCu_4S_3$ ($P4/mmm$), $RbCu_3S_2$ ($C2/m$), $Rb_3Cu_8S_6$ ($C2/m$), and $Rb_3Cu_8Se_6$

TABLE I. Wyckoff positions of $NaCu_5S_3$ with $P6_322$ (FEC-1 orientation) and $P6_3/mcm$ symmetry.

Space group	Site	Wyckoff Position	X	y	z
$P6_322$	Na	$2b$	0	0	1/4
	Cu	$6h$	-0.4854	0.4854	1/4
	Cu	$4f$	2/3	1/3	-0.0247
	S	$6g$	0.6699	0.6699	1/2
	Na	$2b$	0	0	1/2
$P6_3/mcm$	Cu	$6f$	1/2	1/2	1/2
	Cu	$4c$	2/3	1/3	1/4
	S	$6g$	0.672	0.672	3/4

($C2/m$). The theoretically predicted [12] ternary compounds in A-Cu-X systems are as follows: $NaCuS$ ($P6_3/mmc$), $RbCuS$ ($Cmcm$), $RbCuSe$ ($Cmcm$), and $RbCuTe$ ($Pnma$). Most of the achiral alkali metal copper chalcogenide members are cen-trosymmetric compounds exhibiting hidden spin polarization effects [1]. Among them, NaCuS, KCuSe, and KCuTe are predicted to have a hidden Dresselhaus (D-2) effect [1], and the rest are predicted to have hidden Rashba (R-2 & D-2) effect [1]. On the basis of structural symmetry analysis, we have found one compound $NaCu_3Te_2$ ($R3m$) with a polar space group permitting Rashba spin splitting.

APPENDIX C: ELECTRONIC STRUCTURES OF THE CHIRAL COMPOUND NaCu₅S₃ WITHOUT SOC

The crystallographic information of the chiral alkali metal copper chalcogenide compound, $NaCu_5S_3$ ($P6_322$), is given in Table I, along with the corresponding AC structure in space group $P6_3/mcm$. The chiral structure ($P6_322$) given in Table I corresponds to the FEC-1 structure in the main text, which is the experimental phase. Table II lists the lattice constants of the potential substrate InN for applying tensile strain on $NaCu_5S_3$.

Figure 7 shows the evaluated band structure for $NaCu_5S_3$ from DFT + U ($U = 6$ eV) without SOC for comparison with the band structure with SOC in Figs. 6(a) and 6(b), and 8 shows the partial density of states and charge densities of the FEC-1/2 and AC phases in $NaCu_5S_3$ from DFT + U without SOC. The top valence bands of the three phases are mainly formed by hybridized S ($3p_x/p_y$) and Cu ($3d$) states. In the charge densities of $NaCu_5S_3$, there are four empty interstitial sites per unit cell that have the same size for the AC structure. The sizes of the four interstitial sites of the FEC-1/2 structures disproportionate, i.e., half of them increase and

TABLE II. Comparison of lattice constants of potential substrate InN with $NaCu_5S_3$, where a_{sub} and a_{sub}^{opt} represent the primitive and minimal coincident lattice constants of the specified crystal plane.

	a_{sub} (Å)	a_{sub}^{opt} (Å)	Mismatch (%) $|a_{sub}^{opt} - a_{NaCu_5S_3}|/a_{NaCu_5S_3}$	
wz-InN (001)	3.584	7.168 (2×2)	$+2.3$	Tensile

the other half decrease [Fig. 8(b)]. This small change of atomic coordination as well as charge distribution lead to the ferri-chirality. The calculated band gap of $NaCu_5S_3$ from $DFT + U = 6$ eV is almost the same as the band gap from

HSE06 (~0.12 eV). Figure 9 compares the band structures obtained with the two different functionals. The band splitting of the top valence bands is weakly dependent on the U parameter (Fig. 11).

[1] X. Zhang, Q. Liu, J. W. Luo, A. J. Freeman, and A. Zunger, Nat. Phys. **10**, 387 (2014).

[2] D. Di Sante, P. Barone, R. Bertacco, and S. Picozzi, Adv. Mater. **25**, 509 (2013).

[3] G. Dresselhaus, Phys. Rev. **100**, 580 (1955).

[4] J.-W. Luo, G. Bester, and A. Zunger, Phys. Rev. Lett. **102**, 056405 (2009).

[5] H. Mirhosseini, I. V. Maznichenko, S. Abdelouahed, S. Ostanin, A. Ernst, I. Mertig, and J. Henk, Phys. Rev. B **81**, 073406 (2010).

[6] P. S. Halasyamani and K. R. Poeppelmeier, Chem. Mater. **10**, 2753 (1998).

[7] R. Gautier, X. Zhang, L. Hu, L. Yu, Y. Lin, T. O. L. Sunde, D. Chon, K. R. Poeppelmeier, and A. Zunger, Nat. Chem. **7**, 308 (2015).

[8] X. Zhang, V. Stevanović, M. d'Avezac, S. Lany, and A. Zunger, Phys. Rev. B **86**, 014109 (2012).

[9] S. B. Zhang, S.-H. Wei, and A. Zunger, Phys. Rev. Lett. **78**, 4059 (1997).

[10] F. Yan, X. Zhang, Y. G. Yu, L. Yu, A. Nagaraja, T. O. Mason, and A. Zunger, Nat. Commun. **6**, 7308 (2015).

[11] G. Bergerhoff, I. D. Brown, and F. Allen, *Crystallographic Databases* (International Union of Crystallography, Chester, 1987).

[12] X. Zhang, L. Yu, A. Zakutayev, and A. Zunger, Adv. Funct. Mater. **22**, 1425 (2012).

[13] M. J. DeVries Vermeer, X. Zhang, G. Trimarchi, M. D. Donakowski, P. J. Chupas, K. R. Poeppelmeier, and A. Zunger, J. Am. Chem. Soc. **137**, 11383 (2015).

[14] G. Trimarchi, X. Zhang, M. J. D. Vermeer, J. Cantwell, K. R. Poeppelmeier, and A. Zunger, Phys. Rev. B **92**, 165103 (2015).

[15] H. Effenberger and F. Pertlik, Monatsh. Chem. **116**, 921 (1985).

[16] X. Zhang, M. G. Kanatzidis, T. Hogan, and C. R. Kannewurf, J. Am. Chem. Soc. **118**, 693 (1996).

[17] G. Savelsberg and H. Schäfer, Mater. Res. Bull. **16**, 1291 (1981).

[18] Z. Peplinski, D. B. Brown, T. Watt, W. E. Hatfield, and P. Day, Inorg. Chem. **21**, 1752 (1982).

[19] K. O. Klepp, M. Sing, and H. Boller, J. Alloy. Compd. **184**, 265 (1992).

[20] K. O. Klepp, M. Sing, and H. Boller, J. Alloy. Compd. **198**, 25 (1993).

[21] S. L. Dudarev, G. A. Botton, S. Y. Savrasov, C. J. Humphreys, and A. P. Sutton, Phys. Rev. B **57**, 1505 (1998).

[22] P. Błoński and J. Hafner, Phys. Rev. B **79**, 224418 (2009).

[23] J. Heyd, G. E. Scuseria, and M. Ernzerhof, J. Chem. Phys. **124**, 219906 (2006).

[24] J. Heyd, G. E. Scuseria, and M. Ernzerhof, J. Chem. Phys. **118**, 8207 (2003).

[25] K. Murata, M. Aoki, T. Suzuki, T. Harada, H. Kawabata, T. Komori, F. Ohseto, K. Ueda, and S. Shinkai, J. Am. Chem. Soc. **116**, 6664 (1994).

[26] J. J. de Jong, L. N. Lucas, R. M. Kellogg, J. H. van Esch, and B. L. Feringa, Science **304**, 278 (2004).

[27] I. Katsuyoshi, L. Weitao, S. Yuen Ron, U. Hidehiro, O. Yuji, and K. Shin-Ya, J. Chem. Phys. **122**, 141103 (2005).

[28] V. Simic-Milosevic, J. Meyer, and K. Morgenstern, Angew. Chem. Int. Edit. **48**, 4061 (2009).

[29] R. Amaranatha Reddy, M. W. Schröder, M. Bodyagin, H. Kresse, S. Diele, G. Pelzl, and W. Weissflog, Angew. Chem. **44**, 774 (2005).

[30] B. L. Feringa and R. A. Van Delden, Angew. Chem. Int. Edit. **38**, 3418 (1999).

[31] S. S. Skourtis, D. N. Beratan, R. Naaman, A. Nitzan, and D. H. Waldeck, Phys. Rev. Lett. **101**, 238103 (2008).

[32] R. J. Cave, Science **323**, 1435 (2009).

[33] S.-Y. Xu, Q. Ma, Y. Gao, A. Kogar, A. Zong, A. M. M. Valdivia, T. H. Dinh, S.-M. Huang, B. Singh, C.-H. Hsu, T.-R. Chang, J. P. C. Ruff, K. Watanabe, T. Taniguchi, H. Lin, G. Karapetrov, D. Xiao, P. Jarillo-Herrero, and G. Nuh, Nature (London) **578**, 545 (2020).

[34] H. Ohsumi, A. Tokuda, S. Takeshita, M. Takata, M. Suzuki, N. Kawamura, Y. Kousaka, J. Akimitsu, and T. h. Arima, Angew. Chem. Int. Edit. **52**, 8718 (2013).

[35] S.-W. Choi and H. Takezoe, Soft Matter **12**, 7937 (2016).

[36] N. P. M. Huck, W. F. Jager, B. de Lange, and B. L. Feringa, Science **273**, 1686 (1996).

[37] M. Gradhand and J. van Wezel, Phys. Rev. B **92**, 041111(R) (2015).

[38] K. Toyoda, K. Miyamoto, N. Aoki, R. Morita, and T. Omatsu, Nano Lett. **12**, 3645 (2012).

[39] K. Morisawa, T. Ishida, and T. Tatsuma, ACS Nano **14**, 3603 (2020).

[40] W. Kohn and L. J. Sham, Phys. Rev. **140**, A1133 (1965).

[41] G. Kresse and D. Joubert, Phys. Rev. B **59**, 1758 (1999).

[42] J. P. Perdew, K. Burke, and M. Ernzerhof, Phys. Rev. Lett. **77**, 3865 (1996).

[43] G. Kresse and J. Furthmüller, Comput. Mater. Sci. **6**, 15 (1996).

[44] H. J. Monkhorst and J. D. Pack, Phys. Rev. B **13**, 5188 (1976).

[45] G. Henkelman, B. P. Uberuaga, and H. Jónsson, J. Chem. Phys. **113**, 9901 (2000).

[46] K. Momma and F. Izumi, J. Appl. Crystallogr. **44**, 1272 (2011).

[47] W. Jia, Z. Cao, L. Wang, J. Fu, X. Chi, W. Gao, and L.-W. Wang, Comput. Phys. Commun. **184**, 9 (2013).

[48] W. Jia, J. Fu, Z. Cao, L. Wang, X. Chi, W. Gao, and L.-W. Wang, J. Comput. Phys. **251**, 102 (2013).